

# Formation and Dissolution Processes of the 6-Thioguanine (6TG) Self-Assembled Monolayer. A Kinetic Study

Rafael Madueño, Teresa Pineda, José Manuel Sevilla, and Manuel Blázquez\*

Departamento de Química Física y Termodinámica Aplicada, Universidad de Córdoba,  
Campus de Rabanales, Ed. Marie Curie, E-14071 Córdoba, Spain

Received: July 28, 2004; In Final Form: November 17, 2004

This is a report on the kinetics of the destruction and formation processes of the 6-thioguanine self-assembled monolayer (6TG SAM) on a mercury electrode from acid solutions by chronoamperometry. The destruction of the 6TG SAM that has been previously formed under open circuit potential conditions is carried out by stepping the potential from an initial value where the chemisorbed layer is stable up to potentials where the molecules are no longer chemisorbed. The destruction of the SAM has been described by a model that involves three types of contributions: (i) a Langmuir-type adsorption process, (ii) a 2D nucleation mechanism followed by a growth controlled by surface diffusion, and (iii) a 2D nucleation mechanism followed by a growth at a constant rate. The nonlinear fit of the experimental transients by using this procedure allows the quantitative determination of the individual contributions to the overall process. The kinetics of the formation process is studied under electrochemical conditions. The chronoamperometric experiment allows us to monitor the early stages of 6TG SAM formation. The implications of the physisorbed state at low potentials in the type of monolayer formation and destruction processes as well as the influence of temperature are also discussed.

## 1. Introduction

The understanding of the self-assembly of organic molecules to form highly ordered two-dimensional assemblies has attracted considerable attention during the last 15 years.<sup>1–4</sup>

Thiol-functionalized molecules are very interesting systems that are used to form ordered layers on metallic substrates. These molecules adsorb on metals from liquid solutions through a fast, spontaneous electrochemical reaction in which the metal surface oxidizes as the metal–sulfur bond is formed. The formation of the self-assembled monolayer (SAM) can be controlled by electrochemical means. Moreover, electrochemistry can also be used to remove SAMs that have previously been formed.<sup>5</sup> The self-assembly process to form two-dimensional structures implies molecule–metal, molecule–molecule, molecule–environment, and metal–environment interactions.<sup>6</sup>

Our interest in recent years has been the study of SAMs of mercapto-derivatives of nucleobases. The influence that the different types of interactions have on the monolayer stability is one of the major goals in these studies.<sup>7–10</sup>

In a recent paper, we studied the adsorption and phase formation of 6-thioguanine (6TG) at the mercury/aqueous solution interface in an acidic medium by means of cyclic and alternating current (ac) sensitive voltammetry and capacitance–potential curves. The 6TG molecules form two highly ordered

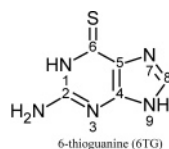
assembled monolayer; in the low potential region, a physisorbed state exists that becomes highly ordered at low temperatures. The regions are separated by a pair of voltammetric peaks that correspond to the formation and destruction of the chemisorbed film and present the characteristics of a 2D condensed phase transition process.<sup>10</sup>

The aim of the present work is the study of the kinetics of the phase transition processes. Both the formation and destruction processes of the 6TG SAM are analyzed in this report. The implications of the physisorbed state at low potentials in the type of monolayer formation and destruction mechanisms are also discussed.

Potential step chronoamperometry is a very convenient technique for studying the kinetics of fast electrode processes. The transients measured contain the information of all the processes taking place in the time scale of the measurement, although the analysis and interpretation of the data is often complicated due to the overlapping of the processes. However, it offers the advantage of an easy interpretation by applying the many different and useful theoretical methods developed.<sup>11–15</sup> Studies dealing with the kinetics of the dissolution of SAMs have appeared recently.<sup>9,16–20</sup> The model of two-dimensional nucleation and growth in which the dissolution of the monolayer is initiated by the creation of etching centers and continues with the reduction of the thiols at the edge of those etching centers has been used in order to explain the presence of the current maximum in the chronoamperometric curves.

## 2. Experimental Section

**2.1. Chemicals.** 6-Thioguanine (6TG) was purchased from Sigma and used without further purification. As the supporting electrolyte, buffered solutions of 0.1–1 M acetic acid and 0.1 M phosphoric acid were used. Milli-Q purified water was used throughout to prepare solutions (17.8–18.2 MΩ·cm, Barnstead System). Pure nitrogen was used for deaerating the working solutions.



monolayers depending on the potential range: in the high potential region, the molecules are chemisorbed and form a self-

\* Corresponding author. E-mail: mblazquez@uco.es. Phone: +34-957-218646. Fax: +34-957-218618.

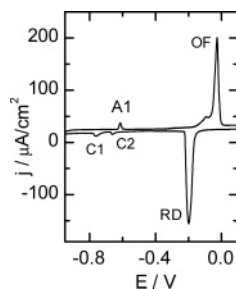


**Figure 1.** Cyclic voltammetry of a 6TG-coated mercury electrode in 0.1 M AcH (pH 4) in  $1 \times 10^{-4}$  M 6TG.  $T = 25^\circ\text{C}$ . Scan rate: 0.1 V/s.

**2.2. Electrodes and Instrumentation.** All electrochemical measurements were performed at a temperature of  $25 \pm 0.1^\circ\text{C}$  (except when the effect of temperature was studied) using a thermostated Metrohm cell in a nitrogen atmosphere.

Cyclic voltammetry and chronoamperometry were recorded on an Autolab (Ecochemie model Pgstat 30) instrument attached to a PC with proper software (GPES and FRA) for total control of the experiments and data acquisition. The instrument was fitted to a 663 VA stand from Metrohm. An HMDE with a surface area of  $0.38\text{ mm}^2$  was used as the working electrode. The reference electrode was an Ag/AgCl/3 M KCl one. The counter electrode was a platinum wire.

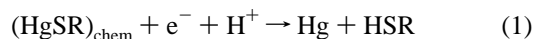
For electrode modification, the mercury drop was exposed to the solution containing 0.1 mM 6TG during a fixed period of time under open circuit potential conditions and the electrochemical measurements were carried out in the presence of the modifier in solution. The electrochemical experiment was run starting with the initial potential which was varied depending on the type of experiment.

### 3. Results and Discussion

Recent results obtained by us have shown the existence of a 2D phase transition process of 6TG molecules at the Hg/aqueous solution interface in an acidic medium.<sup>10</sup>

The presence of an S atom attached to the purine ring derivative addresses the molecule to the spontaneous reaction with the mercury surface atoms. As the 6TG molecules tend to adopt the stacked structure, they suffer an assembly process that should occur simultaneously with the above-mentioned reaction. Hence, the result is the formation of a compact monolayer that precludes that additional 6TG molecules reach the mercury surface. That should be the reason, once the appropriate experimental conditions are reached, the oxidation of the Hg surface atoms by the thiol functions is inhibited.

A cyclic voltammogram of the 6TG–Hg SAM formed after the exposure of a fresh mercury electrode to a 0.1 mM 6TG solution (0.1 M acetic acid, pH 4) for 2 min at an open circuit potential is shown in Figure 1. When the scan is started at 0.1 V and scanned in the negative direction, a region of potential of low and constant current is observed. This region ends where the cathodic peak centered at  $-0.200\text{ V}$  appears. The peak has been assigned to the reductive desorption of the 6TG–Hg SAM. The negligible dependence of both the current density and the differential capacity values on temperature in the potential region positive to this peak is typical of chemisorbed films. Moreover, the charge density involved under the reduction peak ( $70.6 \pm 0.1\text{ }\mu\text{C}/\text{cm}^2$ , value determined by integration of the current density peaks obtained under different scan rates) is in agreement with the reductive desorption of a complete monolayer. The reaction can be written as



In the potential region negative to the peak, the molecules are no longer chemisorbed. However, the results of studies where the dependence on temperature is analyzed show that a physisorbed film exists over a wide potential range within this region. At more negative potentials, the molecules desorb, as is indicated by the coincidence of the differential capacitance values with that obtained in the blank electrolyte. Thus, the region where the 6TG molecules are physisorbed is limited at high potentials by the reductive desorption (RD) peak and at low potentials by peaks C1 or C2, depending on temperature. In the reverse scan, the capacitive peak A1 triggers the adsorption of the 6TG molecules that should remain physisorbed up to the potentials of the formation of the 6TG SAM under electrochemical control (peak OF).<sup>10</sup>

In Figure 2, the potentials of the peaks that limit the above-mentioned regions are plotted against the temperature. Three main regions can be distinguished: regions I, II, and III. Region I corresponds to a state where the molecules do not interact with the electrode surface. Region II, at higher potentials, represents a physisorbed state of 6TG molecules that exists in all of the ranges of temperatures studied. Finally, region III comprises the potentials where the chemisorbed state of 6TG molecules is stable.

The effect of the supporting electrolyte on the interfacial behavior of 6TG has also been studied. In Figure 3, the cyclic voltammograms obtained when the concentration of acetic acid is changed from 0.1 to 1 M, with the rest of the experimental conditions being the same as those in Figure 1, are shown. A cyclic voltammogram recorded in 0.1 M phosphoric acid at pH 4.0 is also plotted. It is interesting to observe that in the potential region where the 6TG SAM is stable, no changes occur. The reductive desorption (RD) peak does not change in potential and shape. These facts agree with the idea that the electrolyte anions are not influencing the SAM properties. However, small changes are observed in region II at the low potential value edge. The cathodic peaks C1 and C2 coalesce, giving only one peak that appears displaced by 90 mV in 1 M acetic acid with respect to peak C2 in 0.1 M acetic acid. Then, the result of an increase in the acetic acid concentration is a slight widening of region II where the physisorbed state of 6TG exists. In the anodic scan, a similar effect is observed, although the sharpening of the peak due to the formation of the 6TG SAM under electrochemical control at a high acetic acid concentration is noticeable. The behavior observed when the nature of the electrolyte is changed by replacing acetic acid by phosphoric acid (Figure 3E) is similar to that in acetic acid, although in this case a small change in the potential ( $\approx 25\text{--}30\text{ mV}$ ) for the reductive desorption peak is obtained.

These experimental results point to the idea that, although the destruction of the SAM is not influenced by the concentration of acetic acid, the physisorbed layer of 6TG molecules in the potential region II is slightly altered by the presence of different concentrations of the electrolyte. The changes observed in the anodic peak could be related either to the differences in the physisorbed state that is previous to the chemisorption reaction or to the differences in the interface environment as the electrolyte concentration is changed.

The kinetics of the transition between the physisorbed and chemisorbed states can be studied by the chronoamperometric technique, using single step potential experiments.

The destruction process of the 6TG SAM has been studied by stepping the potential from an initial value in region III where

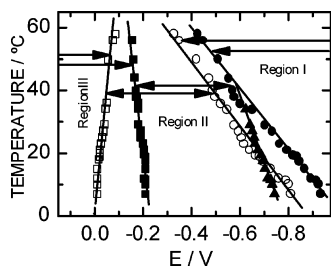


**Figure 2.** Variation of the peak potentials as a function of temperature: (●) C1; (▲) C2; (■) RD; (○) A1; (□) OF.

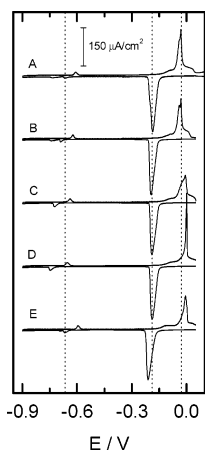


**Figure 3.** Cyclic voltammetry of a 6TG-coated mercury electrode in (A) 0.1 M AcH, (B) 0.2 M AcH, (C) 0.5 M AcH, (D) 1 M AcH, and (E) 0.1 M H<sub>3</sub>PO<sub>4</sub> (pH 4.0) in  $1 \times 10^{-4}$  M 6TG.  $T = 25$  °C. Scan rate: 0.1 V/s.

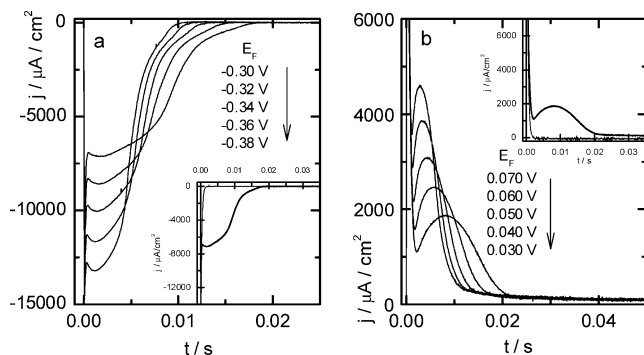


**Figure 4.** (a) Chronoamperometric curves of a 6TG-coated mercury electrode in 0.1 M AcH (pH 4) in  $1 \times 10^{-4}$  M 6TG (RD peak). The monolayer is built up by maintaining the fresh mercury electrode in contact with the 6TG solution for 2 min under an open circuit potential. The initial potential was set at 0 V. The inset shows the current transients obtained at a final potential of  $-0.300$  V for a 6TG-coated mercury electrode (—) and for the blank electrolyte (---). (b) Chronoamperometric curves for the formation of a 6TG monolayer in a mercury electrode in 0.1 M AcH (pH 4) in  $1 \times 10^{-4}$  M 6TG (OF peak). The mercury electrode is allowed to equilibrate at the initial potential ( $-0.5$  V) for a time sufficient to form the physisorbed layer. The inset shows the current transients obtained at a final potential of  $0.030$  V in the presence of 6TG (—) and for the blank electrolyte (---).  $T = 25$  °C.

the SAM, that has been previously formed at an open circuit potential, is stable to a final potential value within region II. Under these conditions, the chronoamperometric curves shown in Figure 4a are obtained. It can be observed that the  $j$ - $t$  curves are characterized by a sharp decay followed by a pronounced maximum and finally by a current decrease. The current density reaches a maximum value at a time,  $t_{\max}$ , that becomes shorter as the potential step increases. Moreover, the maximum current density increases with the potential step. It is worth noting that

the charge density of the transients remains constant independent of the magnitude of the potential jump and is similar to the one involved in the reductive desorption peak in the cyclic voltammogram.

The kinetics of the formation of the 6TG SAM has also been studied by recording the current transient produced by stepping the potential from an initial value within region II to different final values in region III. Figure 4b shows a set of these transients. The initial fast decay of the current density followed by the appearance of a maximum in the  $j$ - $t$  curves, as has been observed for the destruction process, is also obtained in this case. In a similar way,  $t_{\max}$  decreases and  $j_{\max}$  increases as the potential jump becomes larger. The charge density of the transients is independent of the potential step but in all cases is smaller than the one involved in the voltammetric anodic peak.

However, a comparison of parts a and b of Figures 4 evidences a different shape of the current transients obtained for the SAM destruction and formation processes. In fact, the  $j$ - $t$  curves for the destruction show an asymmetric shape that allows us to distinguish a shoulder at times higher than the main current maximum.

The sharp decline in the current is related to the electrode double layer charging effect initiated by the potential pulse employed. In a study of copper underpotential deposition, Hölzle et al.<sup>21</sup> showed that such a charging effect can be correlated quantitatively to the adsorption-desorption process of ions on the electrode surface. The estimation of the contribution due to the double layer charging effect has been based on a Langmuir-type adsorption-desorption equilibrium that can be expressed by eq 2:

$$j_{\text{DL}} = k_1 \exp(-k_2 t) \quad (2)$$

where

$$k_1 = k_2 q_{\text{ads}} \quad (3)$$

and  $q_{\text{ads}}$  is the total charge involved in the adsorption-desorption process. In the case of the transient curves studied in this work, the contribution of this charge is practically the same as that obtained in the blank electrolyte when the rest of the conditions of the experiment are maintained (Figure 4, inset). This contribution can be avoided by a subtraction of the corresponding transient, but it would be more appropriate to include this portion of data in the analysis and perform a fit of the data as they are obtained. Thus, the nonlinear analysis can be made by a sum of terms, with the first of them given by eq 2.

The generalized form of the Bewick-Fleischman-Thirsk (BFT) equation of 2D polynucleation and growth<sup>12</sup> represented by eq 4 is also used in order to analyze the portion of the data showing a current maximum:

$$j(t) = k_a t^{n-1} \exp(-k_b t^n) \quad (4)$$

In eq 4,  $k_a = n q_{\text{nucl}} k_b$ ,  $k_b$  is a coefficient that combines the rates of nucleation and growth,  $n$  is a parameter determined by the kinetic mechanism, and  $q_{\text{nucl}}$  corresponds to the total charge involved in the nucleation process.

The limiting cases of eq 4 are  $n = 2$  for an instantaneous nucleation mechanism and  $n = 3$  for a progressive nucleation mechanism. A comparison between the experimental and theoretical current transients was performed in a nondimensional plot of  $j/j_m$  versus  $t/t_m$  in order to determine the nucleation mechanism from the experimental data. The theoretical current transients for instantaneous and progressive nucleation were



calculated using eqs 5 and 6, respectively:<sup>22</sup>

$$\frac{j}{j_m} = \left(\frac{t}{t_m}\right) \exp\left[-\frac{1}{2}\left(\frac{t^2 - t_m^2}{t_m^2}\right)\right] \quad (5)$$

$$\frac{j}{j_m} = \left(\frac{t}{t_m}\right)^2 \exp\left[-\frac{2}{3}\left(\frac{t^3 - t_m^3}{t_m^3}\right)\right] \quad (6)$$

where  $t_m$  and  $j_m$  are the coordinates of the current maximum and  $t$  is the time of the potential perturbation.

Figure 5 shows experimental data obtained for both the destruction and formation processes compared with the theoretical curves calculated using eqs 5 and 6. The plot of the current transients obtained for the destruction process does not allow us to make a conclusion about the type of nucleation mechanism involved. This result agrees with our expectations, since, as mentioned above, the shape of the curves is asymmetric and should be the result of at least two processes that can run consecutively. However, the formation process follows a shape quite similar to the response predicted for a 2D instantaneous (2DI) nucleation.

To further analyze these curves, a nonlinear fitting procedure has been assayed. The general form of the BFT theory (eq 4) does not give good results in the analysis of the monolayer destruction curves. In fact, the asymmetric form of the transients suggests the occurrence of two processes that should take place consecutively. The possibility of overlapping between those processes can also be taken into account. Using existing theoretical formalisms and the procedure recently developed by Palomar-Pardavé et al.,<sup>23–25</sup> the different processes within the experimentally recorded transients can be recognized and quantitatively determined.

The description with two consecutive 2D nucleation processes being both progressive or instantaneous or one of them progressive and the other instantaneous has not been successful in the fit of the experimental transients obtained for the destruction process. However, if the behavior observed in other systems<sup>26–30</sup> is taken into account, a nucleation process following an exponential law in combination with a surface diffusion controlled growth can be considered. Equation 7 describes this mechanism:

$$j_{SD} = q_{SD}k_g[1 - \exp(-k_n t)] \exp\left[-k_g\left(t - \frac{1}{k_n}[1 - \exp(k_n t)]\right)\right] \quad (7)$$

where  $j_{SD}$  is the current density that corresponds to the process controlled by surface diffusion,  $q_{SD}$  is the charge associated with that contribution,  $k_n$  is the nucleation rate constant, and  $k_g$  is a rate constant related to the growth process.

Equation 8, which takes into account the contributions of the double layer charging effect ( $j_{DL}$ ) (eq 4), that given by eq 7, and a contribution of a progressive nucleation process, has allowed the best fit for the experimental data.

$$j_T = j_{DL} + j_{SD} + j_{PRO} \quad (8)$$

The contribution of  $j_{PRO}$  is given by eq 9 derived by the BFT theory for a 2D progressive nucleation:<sup>22</sup>

$$j_{PRO} = k_3 t^2 \exp(-k_4 t^3) = \frac{\pi n F M h A N_0 k_g^2 t^2}{\rho} \exp\left(-\frac{\pi M^2 A N_0 k_g^2 t^3}{3 \rho^2}\right) \quad (9)$$

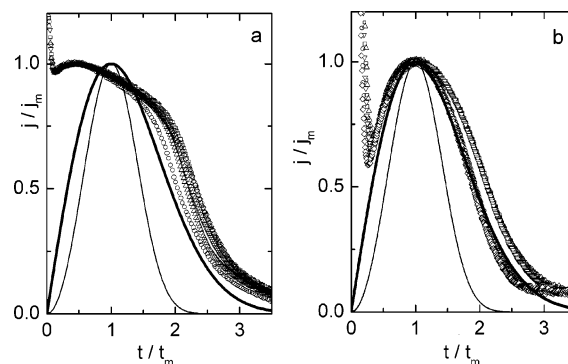


**Figure 5.** Reduced variable plots for the transients shown in Figure 3. The final potentials are as follows: (a) peak RD ( $\diamond$ )  $-0.300$  V, ( $\circ$ )  $-0.320$  V, ( $\nabla$ )  $-0.330$  V, ( $\square$ )  $-0.340$  V, ( $\triangle$ )  $-0.350$  V; (b) peak OF ( $\diamond$ )  $0.030$  V, ( $\circ$ )  $0.035$  V, ( $\nabla$ )  $0.040$  V, ( $\square$ )  $0.045$  V, ( $\triangle$ )  $0.050$  V. The calculated curves for (—) progressive and (---) instantaneous nucleation are included for comparison with the experimental data.

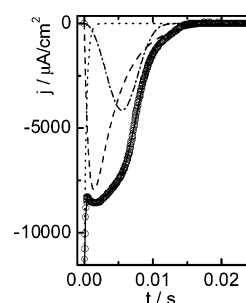


**Figure 6.** 6TG SAM destruction. Experimental current transient ( $\circ$ ) recorded at  $-0.320$  V and a corresponding theoretical curve (—) of the combined nucleation model (eq 8). The individual contributions that form eq 8 are also shown: ( $\cdot \cdot \cdot \cdot \cdot$ ) DL, eq 2; (---) SD, eq 7; (- · - · -) PRO, eq 9.

where  $A$  is the nucleation constant,  $N_0$  is the number density of the active sites,  $k_g$  is the lateral growth rate constant of nuclei,  $M$  is the molecular weight,  $\rho$  is the density of the deposited material,  $nF$  is the molar charge transferred during the electrochemical process, and  $h$  is the height of the deposited layer.

Figure 6 shows a theoretical current transient obtained from eq 8 (full line) which describes the experimental transient recorded at  $-0.320$  V (empty circles). The individual contributions of the different processes (DL, SD, and PRO) are also shown.

The set of kinetic parameters for the theoretical transients which are the best fit for the experimental data obtained at different final potential values are plotted in Figure 7. The fitting procedure used for the contribution due to a progressive nucleation mechanism does not allow us to obtain the individual parameters, as can be done for the first one. As can be observed by analyzing eq 9, only the parameters  $AN_0k_g^2$  can be obtained.

The exponential variation expected for the nucleation rate constant as it is predicted by the atomistic model<sup>31</sup> is well observed only for the  $AN_0k_g^2$  parameters obtained from the component that follows the progressive mechanism. The atomistic model relates the rate of nucleation to that of the formation of the critical nucleus, and the potential dependence is introduced by supposing that the electrochemical driving force is related to the product of the number of atoms in the critical nucleus and the overpotential. In the case of  $k_n$  and  $k_g$ , no such variation is observed but both rate constants increase with overpotential. The charge densities involved under the global and individual contributions to the overall current transients have been obtained by the integration of the representative curves, and the results are plotted in Figure 8.

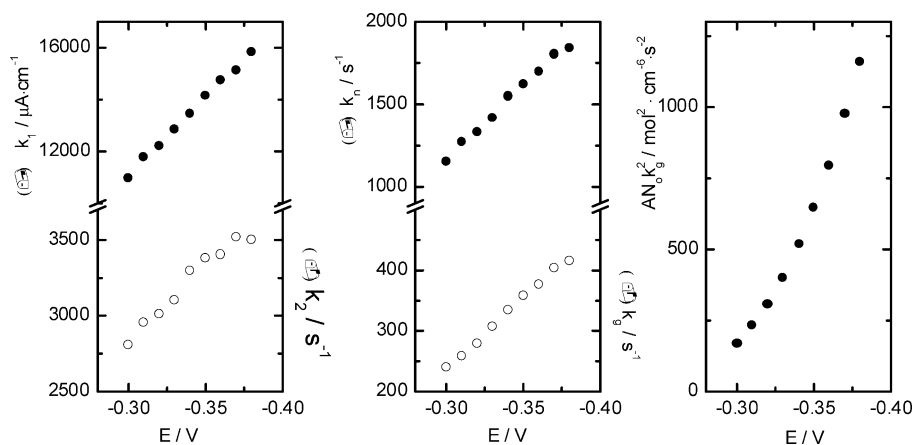


**Figure 7.** Plots of the kinetic parameters as a function of the final potential for the process of destruction of the 6TG–Hg SAM in 0.1 M AcH (pH 4) in  $1 \times 10^{-4}$  M 6TG.

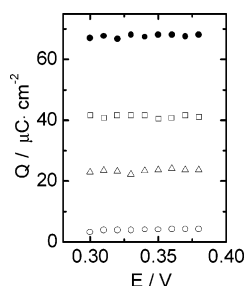


**Figure 8.** Plot of the charge density involved in the transients for the process of destruction of the 6TG–Hg SAM, as a function of the final potential, obtained from the nonlinear fit with eq 8: (●)  $q_T$ ; (○)  $q_{DL}$ ; (□)  $q_{SD}$ ; (△)  $q_{PRO}$ .

It is interesting to see that the total charge involved in the processes and that of the individual contributions remain almost constant independently of the final potential.

A comparison of the results of 6TG with those of the analogue 6-mercaptopurine (6MP) can help in understanding the observed behavior. The comparison of 6TG in alkaline media cannot be made, as the 6TG SAM only exists under acidic conditions.

The destruction of 6MP SAMs has been studied in acidic<sup>7</sup> and alkaline media.<sup>9,32</sup> In an acidic medium, the shape of the  $j-t$  curves is similar to that obtained for 6TG. The curves present an asymmetric shape that should involve at least two different contributions. On the other hand, the  $j-t$  curves obtained in alkaline solutions show a shape that involves a single contribution. A nucleation mechanism following an exponential law combined with a surface diffusion controlled growth as that given by eq 7 has been successful in the fit of the experimental transients in a wide range of step potentials.<sup>32</sup>

Thus, the behavior observed in the acidic medium is different from that found in the alkaline media. It is interesting to point out the differences found in both media in relation with the interface state within the region of potentials negative to the reductive desorption peak. In an alkaline medium, upon reduction of the S–Hg bond, the 6MP molecules are in a situation of weak adsorption at the Hg surface. On the contrary, in an acidic medium, the 6MP molecules form a diluted phase that, under determined experimental conditions, is transformed into a condensed phase of physisorbed molecules that are thought to adopt a flat orientation, according to the results of adenine.<sup>33–37</sup> This is also the case for the interfacial behavior of 6TG under acidic conditions.<sup>10</sup>

In the physisorbed region II (Figure 2), the 6TG molecules can be either coadsorbed with weakly hydrogen-bonded interfacial water giving rise to a low coverage film or interconnected

by directional hydrogen bonds forming a 2D condensed physisorbed film. The role of acetic anions in the formation of these films should not be neglected. In this sense, the changes observed in the voltammograms when the concentration of acetic acid changes point to this direction. However, the destruction process should not be affected by the acetic anions, as the reduction peak does not change.

Chronoamperometric curves for the destruction process in solutions containing different acetic acid concentrations but maintaining the rest of conditions as the same as those in Figure 4 have also been recorded. The transients that show a similar shape of those obtained in 0.1 M acetic acid solutions have been analyzed by using eq 8. The overall charge density as well as the ratio between the individual contributions remains constant with potential for all the acetic acid concentrations used. However, the overall transition time in the transients decreases as the concentration increases.

Results of time-resolved in situ ATR-SEIRAS of adsorption and 2D phase formation of uracil on gold electrodes<sup>38</sup> demonstrate that the transformation of perpendicularly oriented, chemisorbed molecules into lower coverage adlayers proceeds by changes in their orientation toward a tilted or planar arrangement accompanied by the desorption of strongly hydrogen-bonded second layer water and sulfate species and the adsorption of weakly hydrogen-bonded water.

A similar picture for the 6TG molecules chemisorbed on the mercury surface can be taken in mind. Moreover, it can be assumed that the strong stacking interactions between purine rings do not allow the water and acetic acid species to enter the film. However, it is possible, as occurs in uracil chemisorbed on gold,<sup>38</sup> that a second layer of coadsorbed hydrogen-bonded water and acetate species of a variable composition depending on the acetic acid concentration exists.

An analysis of the transients that follow the formation of the 6TG monolayer has also been carried out. As it has been shown in Figure 5, the nondimensional plots of the data are close to that predicted for 2D instantaneous (2DI) nucleation.

Equation 10, derived from the BFT theory, was then used to estimate the major kinetic parameters of the 2D instantaneous nucleation:

$$j_{\text{INS}} = k_s t \exp(-k_6 t^2) = \frac{2\pi n F M h N_0 k_g^2 t}{\rho} \exp\left(-\frac{\pi M^2 N_0 k_g^2 t^2}{\rho^2}\right) \quad (10)$$

In eq 10,  $N_0$  is the number density of the active sites,  $k_g$  is the

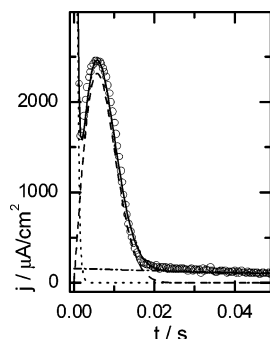


**Figure 9.** 6TG SAM formation. Experimental current transient (O) recorded at  $-0.040$  V and a corresponding theoretical curve (—) of the combined nucleation model (eq 11). The individual contributions that form eq 11 are also shown: (· · · · ·) DL, eq 2; (— — —) INS, eq 10; (— · — · —) ADS, eq 12.

lateral growth rate constant of nuclei,  $M$  is the molecular weight,  $\rho$  is the density of the deposited material,  $nF$  is the molar charge transferred during the SAM formation, and  $h$  is the height of the deposited layer.

Before proceeding with the fitting procedure, it is worth noting that the transient curves for the formation process do not reach the zero current level up to longer times. This fact makes us introduce an additional term in the equation used for the fitting of the experimental data. Then, eq 11 has been used:

$$j_T = j_{DL} + j_{INS} + j_{ADS} \quad (11)$$

where  $j_{DL}$  and  $j_{INS}$  are given by eqs 2 and 10, respectively, and  $j_{ADS}$  is given by eq 12:

$$j_{ADS} = k_7 \exp(-k_8 t) \quad (12)$$

where

$$k_7 = k_8 q_{ADS} \quad (13)$$

and  $q_{ADS}$  is the charge density involved in the process.

Therefore, the experimental current transients shown in Figure 4b were fitted with eq 11 using a nonlinear fitting method. The fitting parameters were  $k_1$  and  $k_2$  (for charging of the double layer),  $k_5$  and  $k_6$  (for the nucleation process under the current maximum), and  $k_7$  and  $k_8$  (for the adsorption process represented by eq 12).

Figure 9 shows a theoretical current transient obtained from eq 11 (full line) which describes the experimental transient recorded at  $-0.040$  V (empty circles). The individual contributions of the different processes (DL, INS, and ADS) are also shown.

The set of kinetic parameters for the theoretical transients which are the best fit for the experimental data obtained at different final potential values are gathered in Table 1. The charge densities involved under the global and individual contributions to the overall current transients have been obtained by the integration of the representative curves, and the results are included in Table 2.

If the structural ideas pointed out above for the physisorbed and chemisorbed states of 6TG molecules in regions II and III, respectively, are taken into account, the behavior observed in the transients for the formation process can be understood. In fact, the 2D instantaneous nucleation and growth process component represents 50% of the overall process. The parallel Langmuir-type contribution to the total current represented by  $q_{ADS}$  corresponds to the adsorption of disordered 6TG molecules that are being incorporated in the film. Whereas the first process

**TABLE 1: Kinetic Parameters of 6TG–Hg SAM Formation for the Current Transients Shown in Figure 3B**

$E_f$ (V)	$k_1$ ( $\mu A \cdot cm^{-2}$ )	$k_2$ ( $s^{-1}$ )	$k_5 (\times 10^{-5})$ ( $\mu A \cdot cm^{-2} \cdot s^{-1}$ )	$k_6 (\times 10^{-4})$ ( $s^{-2}$ )	$k_7$ ( $\mu A \cdot cm^2$ )	$k_8$ ( $s^{-1}$ )
0.020	21355	2225	1.88	0.40	101	3.76
0.025	22010	2282	2.82	0.60	116	4.77
0.030	22177	2320	3.88	0.85	132	5.96
0.035	22980	2368	5.32	1.15	147	7.20
0.040	23352	2406	6.87	1.49	160	8.14
0.045	23706	2457	8.79	1.90	168	8.96
0.050	24034	2513	10.90	2.37	174	9.55
0.055	24625	2564	13.69	2.91	182	9.84
0.060	25128	2630	16.61	3.52	187	10.59
0.070	25801	2695	22.82	4.77	203	11.57

**TABLE 2: Charge Densities for Each of the Processes Contributing to the Formation of the 6TG SAM for Different Step Potentials Used**

$E_f$ (V)	$q_T$ ( $\mu C \cdot cm^{-2}$ )	$q_{DL}$ ( $\mu C \cdot cm^{-2}$ )	$q_{INS}$ ( $\mu C \cdot cm^{-2}$ )	$q_{ADS}$ ( $\mu C \cdot cm^{-2}$ )
0.020	46.1	8.6	23.2	14.3
0.025	46.8	8.6	23.2	15.0
0.030	46.7	8.5	22.7	15.5
0.035	47.3	8.6	23.0	15.7
0.040	47.5	8.6	23.0	15.9
0.045	47.5	8.6	23.1	15.8
0.050	46.9	8.5	22.9	15.5
0.055	47.8	8.6	23.4	15.8
0.060	47.5	8.4	23.5	15.6
0.070	48.0	8.4	23.9	14.7

takes place on a shorter time scale, the second one is slower, as it must involve the reorientation of the molecules upon expulsion of solvent species in order to fulfill complete monolayer formation.

The process of the formation of the 6TG monolayer has also been studied as a function of the acetic acid concentration. As in the case of the destruction process, no changes in the overall behavior have been obtained except for a speedup at higher concentrations. Again, the ratio of acetic anion to water species in the composition of the second layer on top of the 6TG monolayer should be responsible for this higher rate of formation as the acetic acid concentration increases. However, it is necessary to note that the chronoamperometric results do not provide any direct insight into the structural nature of the transitions studied here.

Additional information about the SAM destruction and formation processes can be obtained by an analysis of the chronoamperometric curves as a function of temperature. As mentioned above, the charge density involved in the voltammetric peaks of the processes studied here is almost independent of the temperature. A similar trend is found in the charge density involved in the chronoamperograms taken at different temperatures for the destruction process. However, the charge densities corresponding to the transients recorded for the formation of the 6TG monolayer increase with temperature.

The nonlinear analysis of the transients recorded for the destruction process at different temperatures ( $5$ – $55$  °C) allows a good fitting by using eq 8. Moreover, the contribution of the three components to the overall charge remains the same as that at  $25$  °C. In Figure 10,  $k_g$  and  $k_n$  are plotted against the final potential for the different temperatures studied. An increase of these parameters with temperature is observed that is more important for the nucleation constant. In fact, the increases with both the potential jump and the temperature are more important at higher temperature values.

The values of  $AN_0 k_g^2$  are plotted against the final potential in Figure 11. The same behavior as that for the first contribution is now found.

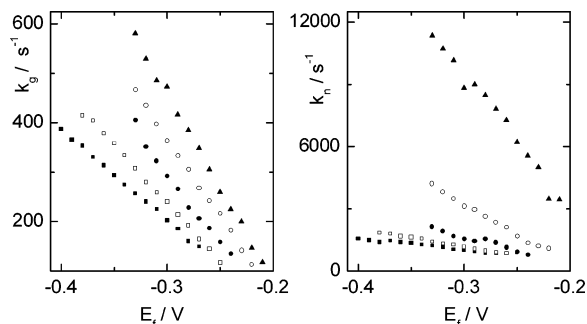


**Figure 10.** Influence of temperature on the nucleation rate constant ( $k_n$ ) and growth parameter ( $k_g$ ) as a function of the final potential for the process of destruction of the 6TG–Hg SAM in 0.1 M AcH (pH 4) in  $1 \times 10^{-4}$  M 6TG: (■) 15 °C; (□) 25 °C; (●) 35 °C; (○) 45 °C; (▲) 55 °C.

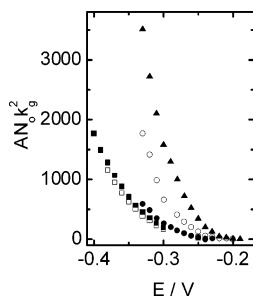


**Figure 11.** Influence of temperature on the kinetic parameters  $AN_0k_g^2$  as a function of the final potential for the process of destruction of the 6TG–Hg SAM in 0.1 M AcH (pH 4) in  $1 \times 10^{-4}$  M 6TG: (■) 15 °C; (□) 25 °C; (●) 35 °C; (○) 45 °C; (▲) 55 °C.

In conclusion, the global destruction process is faster at higher temperatures. This fact is opposite to the finding for the phase transformation of adenosine in different solid amalgam electrode surfaces that is found to be faster at lower temperatures.<sup>39</sup> This last behavior is typical for nonfaradaic condensation processes controlled by a nucleation and growth mechanism<sup>40</sup> and, therefore, follows an opposite behavior than that of the 6TG monolayer destruction that is known to be of faradaic nature.

The transition of 6TG molecules from the physisorbed to the chemisorbed states has also been studied in the range of temperature from 5 to 55 °C. If the BFT model is valid for the experimental results obtained at different temperatures, there must be a linear dependence of  $\log j_{\max}$  and  $\log t_{\max}$  on  $E$  according to eq 14:<sup>21</sup>

$$\frac{\partial(\log j_{\max})}{\partial E} = -\frac{\partial(\log t_{\max})}{\partial E} \quad (14)$$

Figure 12 shows the results of an evaluation of all transients obtained for the formation process as a function of temperature. The slopes of  $\log j_{\max}$  versus  $E$  and  $\log t_{\max}$  versus  $E$  at each temperature value are coincident (see figure captions) even though they increase as the temperature decreases.

An increase of the total charge density involved in the transients with temperature is observed (Figure 13). As it has been found for the destruction, the curves can be fitted by using eq 11 in all the ranges of temperature. The charge density of the different contributions obtained in the fitting analysis is also plotted in Figure 13, where it is interesting to observe that only the contribution of the adsorption process ( $q_{\text{ADS}}$ ) follows an increase with temperature.

For the fitting results of the formation transients, the parameter  $N_0k_g^2$  has been obtained as a function of the potential jump and the temperature. These values are plotted in Figure

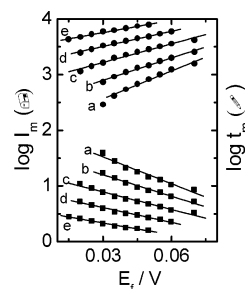


**Figure 12.** Formation of the 6TG–Hg SAM. Influence of temperature on the coordinates of the current maxima in the transients as a function of the final potential: (a)  $T = 5$  °C,  $(\partial \log I_m / \partial E) = 16.6$ ,  $(\partial \log t_m / \partial E) = -16.1$ ; (b)  $T = 15$  °C,  $(\partial \log I_m / \partial E) = 13.4$ ,  $(\partial \log t_m / \partial E) = -12.9$ ; (c)  $T = 25$  °C,  $(\partial \log I_m / \partial E) = 11.1$ ,  $(\partial \log t_m / \partial E) = -10.5$ ; (d)  $T = 35$  °C,  $(\partial \log I_m / \partial E) = 9.1$ ,  $(\partial \log t_m / \partial E) = -8.9$ ; (e)  $T = 45$  °C,  $(\partial \log I_m / \partial E) = 7.4$ ,  $(\partial \log t_m / \partial E) = -7.2$ .

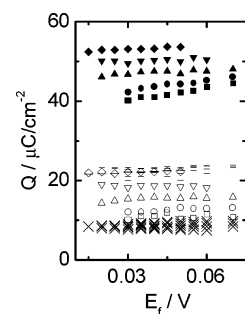


**Figure 13.** Influence of temperature on the charge density involved in the transients obtained in the process of monolayer formation as a function of the final potential. (filled symbols)  $q_T$ : (■) 5 °C; (●) 15 °C; (▲) 25 °C; (▼) 35 °C; (◆) 45 °C. (×)  $q_{DL}$ . (—)  $q_{INS}$ . (empty symbols)  $q_{ADS}$ : (□) 5 °C; (○) 15 °C; (△) 25 °C; (▽) 35 °C; (◇) 45 °C.

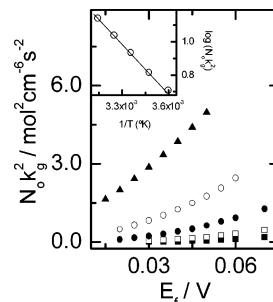


**Figure 14.** Influence of temperature on the kinetic parameter  $N_0k_g^2$  as a function of the final potential for the process of formation of a 6TG–Hg SAM in 0.1 M AcH (pH 4) in  $1 \times 10^{-4}$  M 6TG: (■) 5 °C; (□) 15 °C; (●) 25 °C; (○) 35 °C; (▲) 45 °C. Inset: Plot of  $\log(N_0k_g^2)$  vs  $1/T$ . The data correspond to the transients recorded by stepping the potential from  $-0.5$  to  $-0.045$  V.

14. In a similar fashion of the destruction, the formation process becomes faster by an increase in temperature.

The value of the apparent activation enthalpy ( $E^\ddagger$ ) was estimated by using eq 15:

$$\left[ \frac{\partial \log[N_0k_g^2]}{\partial(1/T)} \right]_{E,c} = -\frac{E^\ddagger}{2.3R} \quad (15)$$

where  $T$  is the temperature in kelvins. The inset of Figure 14 represents the data obtained at  $E_f = -0.045$  V and shows a linear behavior. The slope of this plot allows a value of  $E^\ddagger = 86$  kJ/mol to be determined for the apparent activation enthalpy of the formation process. It is of interest to note that this magnitude is positive, in contrast with the value obtained for the adenine phase transition that is negative.<sup>35–37</sup> The value is



in agreement with processes that take place through the formation of strong bonds with the surface.

#### 4. Conclusions

Cyclic voltammetry and chronoamperometry techniques were used to characterize the kinetic mechanism of 6TG SAM destruction and formation processes on a mercury electrode in acidic solution.

The destruction of the 6TG SAM that has been previously formed on Hg under open circuit potential conditions follows a mechanism involving three contributions: (i) a Langmuir-type adsorption, (ii) a 2D nucleation following an exponential law in combination with a surface diffusion controlled growth, and (iii) a 2D progressive nucleation mechanism followed by a growth process at a constant rate.

The total charge density involved in the overall process coincides with that of the voltammetric peak corresponding to the reductive desorption of the SAM. The fitting procedure employed allows us to obtain the contribution of the three processes mentioned. The different orientation of the 6TG molecules at the chemisorbed and physisorbed states, that is, at the initial and final potentials of the chronoamperometric experiment, together with the influence of solvent species in the monolayer organization, is thought to be responsible for the behavior observed.

The study of the formation of the 6TG SAM requires electrochemical control. Under these conditions, a main process of 2D instantaneous nucleation can be distinguished together with a Langmuir-type adsorption contribution that should represent the slower incorporation of 6TG molecules into the monolayer upon loss of solvent and reorientation.

**Acknowledgment.** We thank the Ministerio de Ciencia y Tecnología (DGI, project BQU 2001-2490), Junta de Andalucía, and University of Córdoba for financial support of this work.

#### References and Notes

- (1) Ulman, A. *An Introduction to Ultrathin Organic Films. From Langmuir-Blodgett to Self-Assembly*; Academic Press: New York, 1991.
- (2) Ulman, A. *Chem. Rev.* **1996**, *96*, 1533–1554.
- (3) Schreiber, A. *Prog. Surf. Sci.* **2000**, *65*, 151–256.
- (4) Ulman, A. *Self-Assembled Monolayers of Thiols*; Thin Films 24; Academic Press: Boston, MA, 1998.
- (5) Finklea, H. O. In *Electroanalytical Chemistry*; Bard, A. J., Rubinstein, I., Eds.; Marcel Dekker: New York, 1996; Vol. 19, p 110.
- (6) Schwartz, D. K. *Annu. Rev. Phys. Chem.* **2001**, *52*, 107–137.
- (7) Sevilla, J. M.; Pineda, T.; Madueño, R.; Roman, A. J.; Blázquez, M. *J. Electroanal. Chem.* **1998**, *442*, 107–112.
- (8) Madueño, R.; Sevilla, J. M.; Pineda, T.; Román, A. J.; Blázquez, M. *J. Electroanal. Chem.* **2001**, *506*, 92–98.

- (9) Madueño, R.; Pineda, T.; Sevilla, J. M.; Blázquez, M. *Langmuir* **2002**, *18*, 3903–3909.
- (10) Madueño, R.; Pineda, T.; Sevilla, J. M.; Blázquez, M. *J. Electroanal. Chem.* **2004**, *565*, 301–310.
- (11) Bewick, A.; Fleischmann, M.; Thirsk, H. R. *Trans. Faraday Soc.* **1962**, *58*, 2200–2216.
- (12) Fleischmann, M.; Thirsk, H. R. In *Advances in Electrochemistry and Electrochemical Engineering*; Delahay, P., Ed.; Wiley: New York, 1963; Vol. 3, pp 123–210.
- (13) Avrami, M. *J. Chem. Phys.* **1937**, *7*, 1103–1112.
- (14) Avrami, M. *J. Chem. Phys.* **1940**, *8*, 212–224.
- (15) Avrami, M. *J. Chem. Phys.* **1941**, *9*, 177–184.
- (16) Calvente, J. J.; Kováčová, Z.; Sánchez, M. D.; Andreu, R.; Fawcett, W. R.; *Langmuir* **1996**, *12*, 5696–5703.
- (17) Yang, D. F.; Morin, M. *J. Electroanal. Chem.* **1997**, *429*, 1–5.
- (18) Yang, D. F.; Morin, M. *J. Electroanal. Chem.* **1998**, *441*, 173–181.
- (19) Vinokurov, I. A.; Morin, M.; Kankare, J. *J. Phys. Chem. B* **2000**, *104*, 5790–5905.
- (20) Vela, M. E.; Martín, H.; Vericat, C.; Andreasen, G.; Hernández-Creus, A.; Salvarezza, R. C. *J. Phys. Chem. B* **2000**, *104*, 11878–11882.
- (21) Hölzle, M. H.; Retter, U.; Kolb, D. M. *J. Electroanal. Chem.* **1994**, *371*, 101–109.
- (22) Thirsk, H. R.; Harrison, J. A. *A Guide to the Study of Electrode Kinetics*; Academic Press: London, 1972; Chapter 3.
- (23) Palomar-Pardavé, M.; Miranda-Hernández, M.; González, I.; Batina, N. *Surf. Sci.* **1998**, *399*, 80–95.
- (24) Palomar-Pardavé, M.; González, I.; Batina, N. *J. Phys. Chem. B* **2000**, *104*, 3545–3555.
- (25) Martínez-Ruiz, A.; Palomar-Pardavé, M.; Valenzuela-Benavides, J.; Farías, M. H.; Batina, N. *J. Phys. Chem. B* **2003**, *107*, 11660–11665.
- (26) Retter, U. *J. Electroanal. Chem.* **1984**, *179*, 25–29.
- (27) Philipp, R.; Dittich, J.; Retter, U.; Müller, E. *J. Electroanal. Chem.* **1998**, *250*, 159–164.
- (28) Van kriecken, M.; Buess-Herman, C. *Electrochim. Acta* **1998**, *43*, 2831–2841.
- (29) Van kriecken, M.; Buess-Herman, C. *Electrochim. Acta* **1999**, *45*, 675–683.
- (30) Mayer, D.; Detschkow, Th.; Ataka, K.; Wandlowski, Th. *J. Electroanal. Chem.* **2002**, *524–525*, 20–35.
- (31) Milchev, A.; Stoyanov, S. *J. Electroanal. Chem.* **1976**, *72*, 33–43.
- (32) Madueño, R.; Pineda, T.; Sevilla, J. M.; Blázquez, M. *J. Electroanal. Chem.*, DOI: 10.1016/j.jelechem.2004.10.016.
- (33) Brabec, V.; Kim, M.; Christian, S.; Dryhurst, G. *J. Electroanal. Chem.* **1979**, *100*, 111–133.
- (34) Prado, C.; Navarro, I.; Rueda, M.; François, H.; Buess-Herman, C. *J. Electroanal. Chem.* **2001**, *500*, 356–364.
- (35) Fontanesi, C. *J. Chem. Soc., Faraday Trans.* **1998**, *94*, 2417–2422.
- (36) Fontanesi, C.; Andreoli, R.; Benedetti, L.; Giovanardi, R.; Ferrarini, P. *Collect. Czech. Chem. Commun.* **2003**, *68*, 1407–1419.
- (37) Benedetti, L.; Camuri, G.; Fontanesi, C.; Ferrarini, P.; Giovanardi, R.; *Electrochim. Acta* **2004**, *49*, 1655–1662.
- (38) Pronkin, S.; Wandlowski, Th. *J. Electroanal. Chem.* **2003**, *550–551*, 131–147.
- (39) Hason, S.; Simonaho, S.-P.; Silvennoinen, E.; Vetterl, V. *J. Electroanal. Chem.* **2004**, *568*, 65–77.
- (40) Buess-Herman, C.; Bare, S.; Poelman, M.; Van Kriecken, M. In *Interfacial Electrochemistry*; Wieckowski, A., Ed.; Marcel Dekker: New York, 1999; p 427.